

Robust Constraints on the Physics of the MeV Emission Line in GRB 221009A from Optical Depth Arguments

Shu-Xu Yi¹*, Zhen Zhang¹, Emre Seyit Yorgancioglu¹, Shuang-Nan Zhang¹, Shao-Lin Xiong¹, Yan-Qiu Zhang¹

¹Key Laboratory of Particle Astrophysics, Institute of High Energy Physics, Chinese Academy of Sciences, Beijing 100049, China

16 September 2024

ABSTRACT

The brightest-of-all-time gamma-ray burst (GRB), GRB 221009A, is the first GRB observed to have emission line (up to 37 MeV) in its prompt emission spectra. It is naturally explained as e^-/e^+ annihilation line that was Doppler boosted in the relativistic jet of the GRB. In this work, we repeatedly apply the simple optical depth argument to different physical processes necessary to produce an observable e^-/e^+ annihilation line. This approach results in robust constraints on the physics of the line: We conclude that in GRB 221009A, the e^-/e^+ pairs were produced at a radius greater than 4.3×10^{15} cm from the central engine, and annihilated in a region between 1.4×10^{16} cm and 4.3×10^{16} cm. From these constraints, we established a self-consistent picture of e^-/e^+ production, cooling, and annihilation. We also derived a criterion for pair production in the GRB prompt emission: $E_{\text{iso}} \gtrsim 3.3 \times 10^{53} E_{\text{peak,100}}(1+z) R_{\text{prod,16}}^2$ erg. Using this criterion, we find tens of candidate GRBs that could have produced e^-/e^+ in prompt emissions to annihilate. GRB 221009A is with the highest likelihood according to this criterion. We also predict the presence of a thermal radiation, with a time-evolving black body temperature, sweeping through soft X-ray during the prompt emission phase.

1 INTRODUCTION

GRB 221009A was observed on the 9th October 2022 with many telescopes, such as *Fermi* (Veres et al. 2022; Lesage et al. 2022), *Insight-HXMT* (Tan et al. 2022), GECAM-C (An et al. 2023), *Swift* (Dichiara et al. 2022), Konus-WIND (Frederiks et al. 2022), *AGILE* (Ursi et al. 2022), *INTEGRAL* (Gotz et al. 2022), GRANDMA (Kann et al. 2023) and LHAASO (Huang et al. 2022). Due to its extraordinary brightness, many detectors suffered from instrumental problems such as data saturation that bias their observation. The dedicated design in detector and read-out electronics of GECAM-C, along with its special operational mode during the burst, allowed it to obtain unbiased data even in the brightest phase of the burst.

The unsaturated and high-resolution GECAM-C data enabled An et al. (2023) to accurately study the spectral and temporal features of this burst and provided a reliable measurement of its record-breaking isotropic equivalent energy E_{iso} as high as 1.5×10^{55} erg. It was identified as the brightest-of-all-time (BOAT) by its peak flux, fluence and E_{iso} , whose event rate was estimated to be once-in-10,000-year (Burns et al. 2023). Additionally, from the observation of the jet break in its early afterglow detected both in keV-MeV by *Insight-HXMT*, GECAM-C and *Fermi*/GBM (An et al. 2023; Zheng et al. 2024) and in TeV by LHAASO (LHAASO Collaboration et al. 2023), the opening angle of the jet was estimated to be $\sim 0.7^\circ$, making it one of the most collimated GRBs ever recorded.

The uniqueness of this burst lies beyond its brightness and narrow jet beam. Ravasio et al. (2023) reported emission line structures in its spectra from 280 s to 360 s after the trigger time in the data of *Fermi*/GBM. The central energy of the emission line was found to be time-varying from about 12 MeV to 6 MeV. Meanwhile, Zhang et al. (2024a) jointly analyzed the data from *Fermi*/GBM and GECAM-C and found emission line structures varying from 37 MeV to 6 MeV from 246 s to 360 s after trigger time. More importantly, thanks to the larger time span of their detection of the emission line, Zhang et al. (2024a) found the central energy of the line evolves as a power-law function with time, with a power-law index of approximately -1, and the flux of the line also evolved as a power-law function with time, with a power-law index of approximately -2. These power-law time-evolution features provide critical evidence that the apparent line structures originate from this GRB rather than from possible instrumental effects or background.

A natural explanation of the observed line is that the MeV line originated from e^-/e^+ annihilation in the relativistic jet, which was Doppler boosted to different observed central energies at different times (see Ravasio et al. 2023; Zhang et al. 2024a,b; however, Wei et al. (2024) proposed a novel model explaining the MeV line as relativistic hydrogen-like heavy ions atomic line). Zhang et al. (2024b) (Zhang24 hereafter) conducted a detailed study based on the e^-/e^+ annihilation framework, where they attributed the time evolution of the line central energy to emission from increasing higher latitude of the jet. According to this assumption, they were able to infer the Lorentz factor and radius of the jet prompt emission region. Zhang24 also essentially excluded some of the alternative mechanisms such as nuclear de-excitation of some radioisotope synthesized during the burst process. Most recently, Pe'er & Zhang (2024) analyses the details of the balanced process

$\gamma + \gamma \leftrightarrow e^+ + e^-$ in order to produce the observed MeV line and deduced constraints on the physics of the source and explained the rarity of such line in GRB.

In this work, we are going to demonstrate that, only if we assume the e^-/e^+ annihilation picture, can we apply the simple optical depth equation repeatedly, namely

$$\tau = nl\sigma = n'l'\sigma,$$

where τ , n , l and σ are the optical depth, number density of particles, geometrical depth and cross section of the corresponding physical process, respectively. The quantities with (without) primes represent those in the comoving (rest) frame, while the cross-section is a Lorentz-invariant. As we will show in the next section, by requiring $\tau > 1$ or $\tau < 1$ for different physical processes, we can obtain many tight constraints on the physical origin of the lines. Such constraints include the positions of the sites of e^-/e^+ annihilation and production. We can see that these constraints are consistent with Zhang24; however, our results are independent of the assumption of high-latitude effects placed in Zhang24 and also independent of the value of the bulk Lorentz factor and the jet opening angle. Based on these inferences, we provide a self-consistent picture from e^-/e^+ production to annihilation. Furthermore, we point out the minimum required E_{iso} needed to produce e^-/e^+ in prompt emission as function of its $E_{\text{peak}}(1+z)$. Our conclusion is that, among tens of other candidates, GRB 221009A has the highest likelihood that there were e^-/e^+ produced in the prompt emission via $\gamma\gamma$ process. In the following section, after we summary our main conclusion on the nature of the line, we discuss on the characteristic of the predicted relic thermal radiation from the equilibrium state of e^-/e^+ production.

2 IMPLICATION ON THE PHYSICAL ORIGIN OF THE EMISSION LINE

2.1 The condition of emergence of the line emission

An emission line can only be observed if the optical depth of the emission region is less than unity. The optical depth caused by the scattering from electrons/positrons are:

$$\tau = 2\sigma_T n'_\pm \delta R'_{\text{line}}, \quad (1)$$

where σ_T is the Thompson scattering cross section, n'_\pm is the number density of e^-/e^+ pairs in the comoving frame, and $\delta R'_{\text{line}}$ is the geometrical width of the line emitting region in the comoving frame. Note that this equation for optical depth is generally valid in GRB 221009A, as the time scale being considered is much shorter than the dynamical time scale (Zhang et al. 2024b; Pe'er & Zhang 2024), required by the narrow line width of $\sim 10\%$, ensuring that the region does not significantly expand. The number density n'_\pm is the ratio between the pair number N_\pm and the comoving volume of the emitting region V' ; the former can be estimated from the observed total energy in the line emission. The total line emission energy in the comoving frame can be calculated as:

$$E'_{\text{line}} = N_\pm m_e c^2 = 4\pi D_L^2 f_b (1+z) \int_{t_i}^{t_f} \frac{\mathcal{F}(t)}{\mathcal{D}(t)} dt, \quad (2)$$

where D_L is the luminosity distance of the GRB, f_b is the beaming factor of the jet, $\mathcal{F}(t)$ is the observed line flux at instant t and $\mathcal{D}(t)$ is the Doppler factor as function of observer's time. The integral is conducted from the initial time t_i to the final time t_f when the line appears. The Doppler factor equals to the ratio between the observed central line energy $\mathcal{E}_{\text{line}}$ and $m_e c^2 = 511 \text{ keV}$. From the observation (Zhang et al. 2024a,b), we know that the observed \mathcal{F} and $\mathcal{E}_{\text{line}}$ evolve with time in power laws, with the reference time $t_0 = 226 \text{ s}$, the power-law indices -2 and -1, and the normalization factors $\mathcal{F}_0 = 0.02 \text{ erg/cm}^2/\text{s}$ and $\mathcal{E}_{\text{line},0} = 8.4 \times 10^5 \text{ keV}$ respectively. Therefore, the above equations can be worked out as:

$$N_\pm = 4\pi D_L^2 f_b (1+z) \frac{\mathcal{F}_0}{\mathcal{E}_{\text{line},0}} \ln \frac{t_f - t_0}{t_i - t_0}. \quad (3)$$

The comoving volume of the emitting region can be estimated as:

$$V' = 4\pi f_b R_{\text{line}}^2 \delta R'_{\text{line}}. \quad (4)$$

Taking the expressions of N_\pm and V' into equation (1), we find

$$\tau = 2\sigma_T D_L^2 (1+z) \frac{\mathcal{F}_0}{\mathcal{E}_{\text{line},0}} \ln \frac{t_f - t_0}{t_i - t_0} R_{\text{line}}^{-2}. \quad (5)$$

The requirement that $\tau < 1$ immediately gives a lower limit of the line emission radius:

$$R_{\text{line}} > \sqrt{2\sigma_T D_L^2 (1+z) \frac{\mathcal{F}_0}{\mathcal{E}_{\text{line},0}} \ln \frac{t_f - t_0}{t_i - t_0}} = 1.4 \times 10^{16} \text{ cm}. \quad (6)$$

We take the values $t_i = 250 \text{ s}$, $t_f = 350 \text{ s}$ (Zhang et al. 2024a), $D_L = 745 \text{ Mpc}$ and $z = 0.151$ (Malesani et al. 2023) in the above calculation. Note that the actual line occurrence duration can be larger than that was observed. Therefore, equation 6 serves as a conservative lower limit.

2.2 The condition of pair annihilation

The annihilation cross section for a pair of free e^-/e^+ in the non-relativistic regime is:

$$\sigma_{\text{anni}} = \frac{3}{8} \sigma_T / \beta_{\text{rel}}, \quad (7)$$

where β_{rel} is the relative velocity between the pair (divided by c). The directional averaged $\beta_{\text{rel}} \sim \beta'_e$, where the latter is the typical velocity of e^-/e^+ in the comoving frame (see Appendix). The effective “optical” depth of e^-/e^+ annihilation can be defined as:

$$\tau_{\text{anni}} = \sigma_{\text{anni}} n'_{\pm} \delta R'_{\text{line}}, \quad (8)$$

where $\tau_{\text{anni}} > 1$ is the region where the e^-/e^+ can annihilate efficiently. Compared with equation (1), one can find that

$$\tau_{\text{anni}} = \frac{3}{16 \beta_{\text{rel}}} \tau. \quad (9)$$

The observation of the line emission indicates that $\tau_{\text{anni}} > 1$ and $\tau < 1$ at the same time, which in return requires $\beta < 3/16 \sim 0.18$. This is in agreement with Zhang24’s statement that, the electrons need to be cooled down to non-relativistic $\beta'_e \sim 0.1$ in order to annihilate efficiently. In Zhang24, the authors found that the cooling from synchrotron radiation and inverse Compton scattering are sufficient to cool down the e^-/e^+ to the required velocity in the comoving frame. However, there lack effective mechanisms to further cool the electrons down to $\beta'_e < 0.01$ in the jet environment, which corresponds to the kinetic energy of tens of electron Volts. We take the expression of τ in equation (5) into equation (9) to find:

$$\tau_{\text{anni}} = \frac{3}{8 \beta_{\text{rel}}} \sigma_T D_L^2 (1+z) \frac{\mathcal{F}_0}{\mathcal{E}_{\text{line},0}} \ln \frac{t_f - t_0}{t_i - t_0} R_{\text{line}}^{-2}. \quad (10)$$

In the above equation, we insert the condition that $\tau_{\text{anni}} > 1$ and $\beta_{\text{rel}} > 0.01$ to obtain another limit on R_{line} :

$$R_{\text{line}} < \sqrt{\frac{3}{8} \times 100 \sigma_T D_L^2 (1+z) \frac{\mathcal{F}_0}{\mathcal{E}_{\text{line},0}} \ln \frac{t_f - t_0}{t_i - t_0}} = 4.3 \times 10^{16} \text{ cm}. \quad (11)$$

Therefore, we see from the simple arguments on the condition of optical depth, we can already set a quite stringent constraint on the location of the e^-/e^+ annihilation to be between 1.4×10^{16} cm and 4.3×10^{16} cm, which is in agreement with the conclusion of Zhang24. However, our conclusion does not depend on the value of the bulk Lorentz factor and the opening angle of the jet. Note that the exact numbers for the upper and lower limits should take into account the observation uncertainties of all the quantities in equations (6) and (11), which is not done here for the numbers will not be significantly changed.

2.3 The origin of e^+/e^- pairs

Denote the radius where the e^-/e^+ were produced and started to transmit freely as R_{prod} . Then τ_{anni} should be less than unity in the range from R_{prod} to R_{line} , in order that the pairs would not be exhausted before R_{line} . Therefore, similar to equation (10), we have:

$$\tau_{\text{anni}} = \frac{3}{8 \beta_{\text{rel},0}} \sigma_T D_L^2 (1+z) \frac{\mathcal{F}_0}{\mathcal{E}_{\text{line},0}} \ln \frac{t_f - t_0}{t_i - t_0} R_{\text{prod}}^{-2} < 1, \quad (12)$$

where $\beta_{\text{rel},0}$ is the relative velocity between e^-/e^+ before the fast cooling. We thus have

$$R_{\text{prod}} > \sqrt{\frac{3}{8 \beta_{\text{rel},0}} \times \sigma_T D_L^2 (1+z) \frac{\mathcal{F}_0}{\mathcal{E}_{\text{line},0}} \ln \frac{t_f - t_0}{t_i - t_0}} \quad (13)$$

$$> \sqrt{\frac{3}{8} \sigma_T D_L^2 (1+z) \frac{\mathcal{F}_0}{\mathcal{E}_{\text{line},0}} \ln \frac{t_f - t_0}{t_i - t_0}} \quad (14)$$

$$= 4.3 \times 10^{15} \text{ cm}. \quad (15)$$

This indicates that the pairs were produced from a region far from the centre engine and well above the photosphere ($\sim 10^{13}$ cm). In Zhang24, e^-/e^+ were assumed to be produced by $\gamma\gamma$ process in the prompt emission region. This assumption is again consistent with our implication on R_{prod} . If $N_{\gamma,0}$ is the number of photons in the initial prompt emission, and a fraction of them η participate in the $\gamma\gamma$ process. Then the number density of those photons is:

$$\begin{aligned} n'_{\gamma} &= \eta N_{\gamma,0} / V'_{\text{prod}} \\ &= \frac{\eta N_{\gamma,0}}{f_b R_{\text{prod}}^2 \delta R'_{\text{prod}}}. \end{aligned} \quad (16)$$

The optical depth of $\gamma\gamma$ pair production is:

$$\begin{aligned} \tau_{\gamma\gamma} &= \sigma_{\gamma\gamma} n'_{\gamma} \delta R'_{\text{prod}} \\ &= \sigma_{\gamma\gamma} \eta N_{\gamma,0} f_b^{-1} R_{\text{prod}}^{-2}, \end{aligned} \quad (17)$$

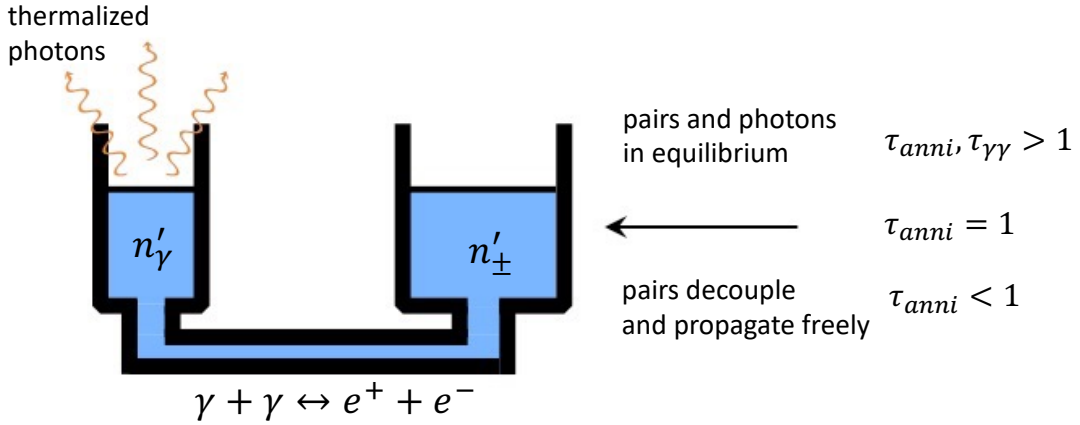


Figure 1. In this cartoon illustration, we draw an analogy between the equilibrium process of e^-/e^+ production/annihilation and a hydrostatic equilibrium system with two connected beakers. The liquid volume on the left represents the number density of high-energy photons involved in pair production n'_γ , while that on the right represents n'_{\pm} . In such a hydrostatic equilibrium system, the liquid levels on both sides remain consistent, analogous to n'_γ and n'_{\pm} tracking each other in equilibrium. The reduction of the liquid on the left due to evaporation analogous to the decrease in high-energy photons due to thermalization. During this process, the liquid representing n'_{\pm} on the right also decreases. When the liquid level drops below the mark labeled $\tau_{\text{anni}} = 1$, the electron-positron pairs decouple from the equilibrium state (Ruffini et al. 1999, 2000; Bianco et al. 2001) and begin to propagate freely.

which is required to be larger than unity. The fraction η is determined by the initial photon spectrum $n'_\gamma(v')$. We emphasize here that, the correspondence between the initial spectrum and the observed spectrum can be complicated since the pair production process altered the initial spectrum. A number of photons $\eta N_{\gamma,0}$ will be converted into e^-/e^+ pairs, and the number of these initially produced pairs equals $N_{\pm,0} = \eta N_{\gamma,0}$. In the centre-of-momentum frame of the pair, the cross section σ_{anni} can be written as (Zhang 2019):

$$\sigma_{\text{anni}} = \frac{3}{8} \sigma_T \frac{1}{\gamma'_e + 1} \left[\frac{\left(\gamma'^2 + 4\gamma'_e + 1 \right) \text{Log} \left(\sqrt{\gamma'^2 - 1} + \gamma'_e \right)}{\gamma'^2 - 1} - \frac{\gamma'_e + 3}{\sqrt{\gamma'^2 - 1}} \right], \quad (18)$$

where $\gamma'_e = (1 - \beta_{\text{rel}}^2)^{-1/2} \simeq (1 - \beta_e^2)^{-1/2}$. Correspondingly the cross section of the inverse process,

$$\sigma_{\gamma\gamma} = \frac{3}{8} \sigma_T \gamma'^2 \left[- \left(-\frac{1}{\gamma'^4} + \frac{2}{\gamma'^2} + 2 \right) \text{Log} \left(\left| \gamma'_e - \sqrt{\gamma'^2 - 1} \right| \right) + \sqrt{1 - \frac{1}{\gamma'^2}} \left(\frac{1}{\gamma'^2} + 1 \right) \right], \quad (19)$$

where $\gamma'_e \equiv h\nu'/m_e c^2$. In the relativistic limit of $\beta'_e \sim 1$, $\sigma_{\text{anni}}/\sigma_{\gamma\gamma} \sim 0.4\gamma'_e$, while in the non-relativistic limit of $\beta'_e \ll 1$, $\sigma_{\text{anni}}/\sigma_{\gamma\gamma} \sim \beta'^{-2}_e$. Roughly, $\sigma_{\text{anni}}/\sigma_{\gamma\gamma} \sim \text{Max}(\beta'^{-2}_e, 0.4\gamma'_e)$. Consequently, the cross section $\sigma_{\gamma\gamma}$ of $\gamma\gamma \rightarrow e^+/e^-$ tends to be less than that of the inverse process, and the produced pairs will immediately undergo the annihilation process. Therefore, there should be a balance process between the pair production and annihilation, until the optical depth of interaction becomes less than unity (Ruffini et al. 1999, 2000; Bianco et al. 2001). In the state of equilibrium, according to the Boltzmann equation, we expect:

$$n'^2_\gamma \sigma_{\gamma\gamma} \sim 2 n'^2_{\pm} \sigma_{\text{anni}} \beta'_e \iff n'_\gamma \sim n'_{\pm} \sqrt{2 \text{Max} \left(0.4\gamma'_e, \frac{1}{\beta'_e} \right)}. \quad (20)$$

In the above equation, we denote the number density of photons which satisfy the condition of pair production as n'_γ . The number density of e^-/e^+ n'_{\pm} thus tracks n'_γ (see also Pe'er & Zhang 2024). Nevertheless, this fraction of photons was in equilibrium with electrons and positrons and eventually cooled to lower energies and finally the pair production ceases. Consequently, n'_{\pm} and n'_γ decrease until the pair production and annihilation process stops and decouple. We illustrate the above process in figure 1.

After this process, the initial photon spectrum is altered: its high energy end is converted into e^-/e^+ and the thermalized photons appear at much lower energies. In figure 2, we present the illustration of this process: The initial spectrum of the prompt radiation in the comoving frame is illustrated in the upper panel. A fraction η of these photons underwent the pair production/annihilation process, so that roughly a half of these photons are converted into e^-/e^+ , while the rest of them are thermalized and contribute to a thermal radiation in the observed prompt emission spectrum in the lower panel. We will discuss the observational prospect of the thermal radiation in the next section.

Given an initial photon spectrum from detailed simulation, (as that illustrated in the upper panel of figure 2, where the second bump at high energy can arise from the Self-Synchrotron Comptonization (SSC)), the fraction of photons which satisfy the pair production condition can be found with a Monte Carlo simulation, together with their total energy. The resulted number of e^-/e^+ , the temperature of thermalized photons and the resulted prompt emission spectrum can thus calculated. A fitting with the simulated spectrum and the observed one can be used to set constraints on the detailed physics conditions. Such a study is beyond the scope of this paper, and will be conducted in a follow up work.

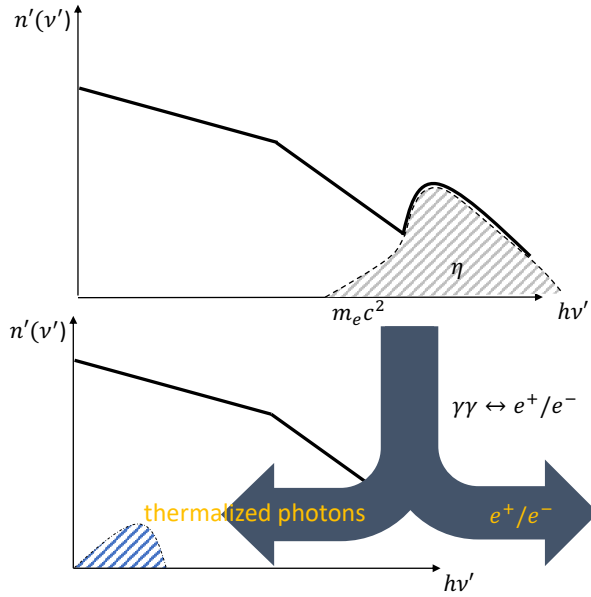


Figure 2. The illustration of the pair production process. The initial spectrum of prompt radiation in the comoving frame is illustrated in the upper panel. A fraction η of these photons underwent the pair production/annihilation process, so that roughly a half of these photons are converted into e^-/e^+ , while the rest of them are thermalized and contributing to a thermal component in the observed prompt emission spectrum in the lower panel.

2.4 The lower limit of E_{iso} for sufficient pair production

The rest of initial photons which do not participate the pair production will largely contribute to the observed prompt emission. The number of photons in the prompt emission can be approximated with $E'_{\gamma, \text{prompt}}/E'_{\text{peak}}$, where $E'_{\gamma, \text{prompt}}$ is the total energy in the prompt emission in the comoving frame and E'_{peak} is the peak energy of the spectrum in the comoving frame, representing an average of $h\nu'$. Since the number of photons is a Lorentz invariance, it also equals $E_{\gamma, \text{prompt}}/(E_{\text{peak}}(1+z)) = E_{\text{iso}}f_b/(E_{\text{peak}}(1+z))$. We therefore have the relation:

$$(1-\eta)N_{\gamma,0} \approx E_{\text{iso}}f_b/(E_{\text{peak}}(1+z)). \quad (21)$$

Taking equation (21) into the expression of $\tau_{\gamma\gamma}$ into equation (17), we find that:

$$\tau_{\gamma\gamma} = \sigma_{\gamma\gamma} \frac{\eta}{1-\eta} \frac{E_{\text{iso}}}{E_{\text{peak}}(1+z)} R_{\text{prod}}^{-2} > 1. \quad (22)$$

The above inequality can be used to set a lower limit of the E_{iso} of GRB which can produce e^-/e^+ :

$$\begin{aligned} E_{\text{iso}} &> E_{\text{peak}}(1+z) \frac{1-\eta}{\eta} \sigma_{\gamma\gamma}^{-1} R_{\text{prod}}^2 \\ &\gtrsim 1.39 E_{\text{peak}}(1+z) \frac{1-\eta}{\eta} \sigma_{\text{T}}^{-1} R_{\text{prod}}^2, \end{aligned} \quad (23)$$

as the maximum value of $\sigma_{\gamma\gamma}$ is about 0.72 σ_{T} . Now, suppose the energy in the photons which participated the pair production is less than $\sim 10\%$ of those which did not (which can be demonstrated via detailed simulation). The former are photons with $h\nu' \gtrsim \text{MeV}$ (so that $h\nu'_1 + h\nu'_2 > 2m_ec^2$), and the latter are those with $h\nu' \sim \text{keV}$ ($E'_{\text{peak}} \sim \text{keV}$). As a result, the number ratio $\eta/(1-\eta)$ between them, should be less than 10^{-4} . We take $\eta/(1-\eta) \lesssim 10^{-4}$ into the above lower limit of E_{iso} to obtain:

$$E_{\text{iso}} \gtrsim 3.3 \times 10^{53} E_{\text{peak,100}}(1+z) R_{\text{prod,16}}^2 \text{ erg}, \quad (24)$$

where $R_{\text{prod,16}}$ is R_{prod} in unit of 10^{16} cm , and $E_{\text{peak,100}}$ is the observed E_{peak} in unit of 100 keV. Equation (24) gives a limit in the parameters space of the Amati relation ($E_{\text{iso}}-E_{\text{peak}}(1+z)$), where e^-/e^+ production in GRB prompt emission is only possible in those sources above this limit (see figure 3). As we can see from figure 3, there are a few candidates lie beyond the limit line when $R_{\text{prod,16}} = 1$, and there are tens of candidates when $R_{\text{prod,16}} = 0.3$. We list these candidates in tables B1 and B2. It should be note that, passing the criterion (equation 24) alone does not guarantee annihilation line be observed in those GRBs, for there are more requirements such as fast cooling, efficient annihilation and optically thin conditions for the line photons to emerge. Furthermore, even if the line emission emerge from a GRB, its luminosity still needs to be high enough to be detected.

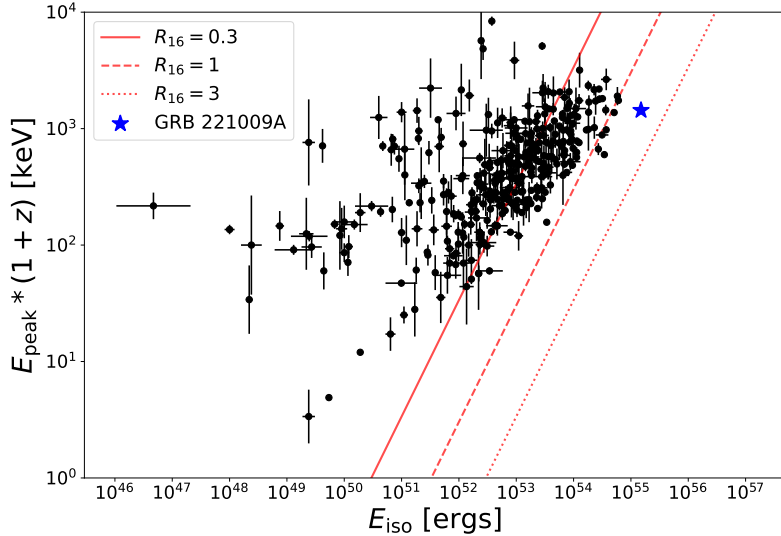


Figure 3. The dashed line represents the $E_{\text{iso}}-E_{\text{peak}}(1+z)$ parameter space constraints set by equation (24), with $R_{\text{prod},16}=0.3, 1, 3$. The data are taken from An et al. 2023.

3 CONCLUSION AND DISCUSSION

3.1 Summaries on the conclusions and physical scenario of pair production and annihilation

In the above section, we took arguments on the optical depths of several physical process, and drew conclusions based on them:

- The line emission region should be optically thin, otherwise the annihilation line will not emerge $\rightarrow R_{\text{line}} > 1.4 \times 10^{16} \text{ cm}$;
- The annihilation optical depth between e^-/e^+ should be larger than unity, in order to effectively produce the line; besides, e^-/e^+ cannot be efficiently cooled down to $\beta'_e < 0.01 \rightarrow R_{\text{line}} < 4.3 \times 10^{16} \text{ cm}$;
- In the location R_{prod} where e^-/e^+ are produced, the annihilation optical depth between e^-/e^+ should be less than unity, otherwise the pairs will not be preserved to $R_{\text{line}} \rightarrow R_{\text{prod}} > 4.3 \times 10^{15} \text{ cm}$;
- The optical depth of $\gamma\gamma \rightarrow e^-/e^+$ needs to be larger than unity in the prompt emission region, in order to produce $e^-/e^+ \rightarrow$ A GRB needs to be bright enough that $E_{\text{iso}} \gtrsim 3.5 \times 10^{53} E_{\text{peak},100}(1+z) R_{\text{prod},16}^2 \text{ erg}$ to have e^-/e^+ annihilation production. Candidate GRBs that could have e^-/e^+ produced in their prompt emission are listed in tables B1 and B2.

The complete scenario of the e^-/e^+ production and emission of the annihilation line is summarized as follows:

- (i) The prompt emission photons are radiated at a radius $\sim 10^{15} \text{ cm}$. In these photons, a fraction of them satisfy the condition that $h\nu'_1 + h\nu'_2 \geq 2m_e c^2$ in the jet comoving frame.
- (ii) The number of those high energy portion of photons are so large that they can efficiently produce e^-/e^+ . e^-/e^+ and the high energy photons are in an equilibrium state of the pair production/annihilation process. Therefore, the number density of e^-/e^+ tracks that of the high energy photons.
- (iii) The equilibrium $\gamma\gamma \leftrightarrow e^-/e^+$ process thermalize those high energy portion of photons, and the number density of e^-/e^+ decreases to unity, when the annihilation is no longer efficient.
- (iv) e^-/e^+ propagates from this distance R_{prod} to a larger distance R_{line} . During the course, the e^-/e^+ is cooled down due to synchrotron or inverse Compton radiation.
- (v) e^-/e^+ is cooled down to a critical β'_e in the comoving frame, so that the annihilation process become efficient again.
- (vi) e^-/e^+ annihilate fast, and the emitted photons can freely escape to infinity due to the optically thin environment.

The above scenario is depicted in figure 4.

It takes $\Delta T_{\text{dyn}} \approx (R_{\text{line}} - R_{\text{prod}})/(\beta'_e c)$ for the pairs to propagate from R_{prod} to their annihilation site R_{line} . This corresponds to a observed time delay $\delta t_{\text{dyn}} = (1+z)\Delta T_{\text{dyn}}/\Gamma^2 \sim 10 \text{ s}$, which is in agreement with the observation that, the time lag between the prompt emission peak and the first occurrence of the line is $\sim 10 \text{ s}$.

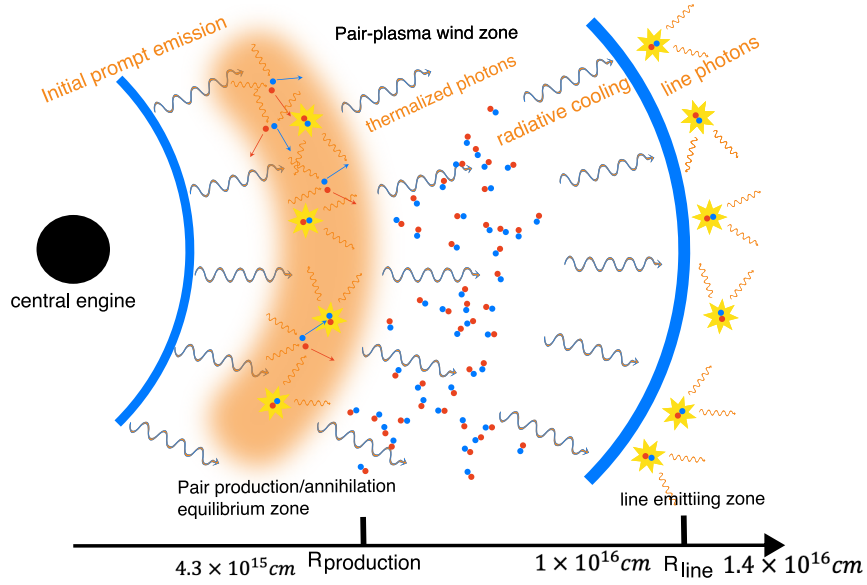


Figure 4. The schematic of the physical processes of the production of e^-/e^+ annihilation line emission.

3.2 Prediction on the relic thermal radiation from pair production

As mentioned above, a major prediction of this scenario is that there should be a thermal component emerging between the epochs of the peak prompt emission and the appearance of line emission. The energy density of the thermalised photons in the comoving frame is equal to that of the photons that participated in e^-/e^+ production:

$$\epsilon' \sim n'_\gamma h\nu', \quad (25)$$

where $h\nu'$ denotes the averaged energy of pair producing photons. According to equation (20), which relates n'_γ with n'_\pm , the energy density can be further expressed as:

$$\epsilon' \sim n'_\pm \gamma_e'^{3/2} m_e c^2, \quad (26)$$

where, again, $\gamma_e' \equiv h\nu'/m_e c^2$. On the other hand, the corresponding black body radiation temperature T' is related with the energy density ϵ' as:

$$\epsilon' = aT'^4, \quad (27)$$

where a is related to the Stefan-Boltzmann constant σ as: $a = 4\sigma/c$. As a result, we can infer that the temperature of the thermal component in the comoving frame is that:

$$T' = \left(n'_\pm \gamma_e'^{3/2} m_e c^2 / a \right)^{1/4}. \quad (28)$$

The peak luminosity of this thermal component is then:

$$\begin{aligned} L_{\text{th,peak}} &= \delta\Omega R_{\text{prod}}^2 \sigma T'^4 \Gamma^2 = (1/\Gamma)^2 R_{\text{prod}}^2 \sigma T'^4 \Gamma^2 \\ &= \frac{1}{4} R_{\text{prod}}^2 c n'_\pm \gamma_e'^{3/2} m_e c^2 \\ &= \frac{1}{4} R_{\text{prod}}^2 c \gamma_e'^{3/2} m_e c^2 \frac{N_\pm}{V'}, \end{aligned} \quad (29)$$

where $\delta\Omega = 1/\Gamma^2$ is the solid angle over which the thermal radiation body is observable due to Doppler beaming effect. Taking the expressions of N_\pm and V' (substituting R_{line} with R_{prod}) in equations (3) and (4), one further expresses $L_{\text{th,peak}}$ as:

$$L_{\text{th,peak}} = \frac{c \gamma_e'^{3/2} m_e c^2 (1+z)}{4 R'_{\text{prod}}} \frac{\mathcal{F}_0}{\mathcal{E}_{\text{line},0}} \ln \frac{t_f - t_0}{t_i - t_0} D_L^2. \quad (30)$$

As $\delta R'_{\text{prod}}$ is the width of the pair production zone in the comoving frame, it is related to that in the rest frame $\delta R'_{\text{prod}}$ with $\delta R'_{\text{prod}} = \Gamma \delta R_{\text{prod}}$. Taking numerical values into equations (28) and (30), one can get that: $T' = 1.38 \times 10^4 \gamma_{e,100}'^{3/8}$ K, where $\gamma_{e,100}'$ is γ_e' in unit of 100. Therefore, the maximum Doppler boosted temperature of the thermal component is $T = (1+z) \Gamma T' \sim 0.1 - 1$ keV, whose radiation is in the soft X-ray band to be distinguished from the photospheric thermal emission of a GRB at much higher energies. The peak luminosity is $L_{\text{th,peak}} = 2 \times 10^{44} \gamma_{e,100}'^{3/2} \delta R_{\text{prod},16}$ erg/s. Correspondingly, the peak flux is $F_{\text{th,peak}} = 3.0 \times 10^{-12} \gamma_{e,100}'^{3/2} \delta R_{\text{prod},16}$ erg/cm²/s. As in Zhang24, the authors explain the apparent line centre energy evolution as a result of the high-latitude effect. Similar effect will also change

the thermal radiation, making the apparent temperature of the thermal component evolve with time $kT \propto (t - t_0)^{-1}$, and its flux evolves with $F_{\text{th}}(t) \propto (t - t_0)^{-3}$ (Kumar & Panaiteescu 2000; Salafia et al. 2015). Therefore, we expect the thermal radiation to sweep through \sim keV to \sim 0.1 keV in soft X-ray band in tens of seconds, with its flux decreasing from $\sim 10^{-12}$ to $\sim 10^{-15}$ erg/cm²/s. The flux is roughly comparable to that of $\sim 10^{-13}$ erg/cm²/s (in 100 s at 0.5-2 keV) achieved by near future telescopes like Athena/WFI (Piro et al. 2014). Nevertheless, such a signal is short duration transient, thus its detection is far below the sensitivity of the current all-sky soft X-ray monitor such as the Wide-field X-ray Telescope (WXT) onboard the Einstein Probe (Yuan et al. 2022) or any all-sky soft X-ray monitor to be deployed in a foreseeable future.

4 DATA AVAILABILITY

No new data were generated or analysed in support of this research.

ACKNOWLEDGMENTS

YSX would like to thank useful discussion over this topic with Profs. Bing Zhang and Zhuo Li. This work is supported by the fund from the Chinese Academy of Sciences (grant Nos. E329A3M1 and E3545KU2)

APPENDIX A: THE RELATIVE VELOCITY BETWEEN TWO RELATIVISTIC PARTICLES

The relative velocity between two particles (with velocities β_1, β_2) is (Landau & Lifshitz 2002):

$$\beta_{\text{rel}}^2 = \frac{\beta_1^2 + \beta_2^2 - 2\beta_1\beta_2 \cos \theta - \beta_1^2\beta_2^2 \sin^2 \theta}{(1 - \beta_1\beta_2 \cos \theta)^2}. \quad (\text{A1})$$

Integration of the above equation over the solid angle gives the directional averaged relative velocity:

$$\bar{\beta}_{\text{rel}}^2 = \frac{1}{2} \int_0^\pi \beta_{\text{rel}}^2 \sin \theta d\theta = \frac{\beta_1^2 + \beta_2^2 - 2\beta_1^2\beta_2^2}{1 - \beta_1^2\beta_2^2}. \quad (\text{A2})$$

Therefore, if all particles have the same velocity β'_e , one finds:

$$\bar{\beta}_{\text{rel}}^2 = 2 \frac{\beta'_e^2}{1 + \beta'_e^2}. \quad (\text{A3})$$

Table B1. GRB candidates which could have e^-/e^+ production in their prompt emission stages, according to criterion equation (24), assuming $R_{\text{prod},16} = 1$

GRB	z	T_{90} (s)	$E_{p,i}$ (keV)	E_{iso} (10^{52} erg)	Detector
110918A	0.98	19.60	667.0	270.50	FER
130907A	1.23	360.00	882.0	314.00	FER
160625B	1.40	454.67	1374.0	510.10	FER
180914B	1.09	272.48	977.0	370.00	KW
190530A	0.93	18.43	1745.0	605.00	FER
210619B	1.93	54.79	598.0	344.00	FER
221009A	0.15	600.00	1436.0	1500.00	FER/KW/HXMT/GECAM

Notes: Column (1): GRB name. Column (2): redshift. Column (3): value of T_{90} . Column (4): isotropic γ -ray energy in rest-frame between $1 - 10^4$ keV. Column (5): Peak energy in rest frame (intrinsic). Column (6): the experiment, used for the measurement of T_{90} , E_p , and E_{iso} values (FER = Fermi, KW = Konus-Wind, SWI = Swift, HXMT = Hard X-ray Modulation Telescope, GECAM = Gravitational wave high-energy Electromagnetic Counterpart All-sky Monitor). Data taken from [An et al. \(2023\)](#).

APPENDIX B: CANDIDATES THAT COULD HAVE e^-/e^+ PRODUCED IN THEIR PROMPT EMISSION

In this appendix section, we give tables B1 and B2 of GRB candidates that could have e^-/e^+ production in their prompt emission stages, according to criterion equation (24).

Notes: Excludes GRBs already satisfying constraints set by $R_{\text{prod},16} = 1$. Column (1): GRB name. Column (2): redshift. Column (3): value of T_{90} . Column (4): isotropic γ -ray energy in rest-frame between $1 - 10^4$ keV. Column (5): Peak energy in rest frame (intrinsic). Column (6): the experiment, used for the measurement of T_{90} , E_p , and E_{iso} values (GRO = CGRO/BATSE, FER = Fermi, KW = Konus-Wind, SWI = Swift, HXMT = Hard X-ray Modulation Telescope, GECAM = Gravitational wave high-energy Electromagnetic Counterpart All-sky Monitor). Data taken from [An et al. \(2023\)](#).

REFERENCES

An, Z.-H., Antier, S., Bi, X.-Z., et al. 2023, arXiv:2303.01203. doi:10.48550/arXiv.2303.01203

Bianco, C. L., Ruffini, R., & Xue, S.-S. 2001, *Astron. Astrophys.*, 368, 377.

Bissaldi, E., Omodei, N., Kerr, M., & Fermi-LAT Team. "GRB 221009A or Swift J1913.1+1946: Fermi-LAT detection." GRB Coordinates Network, no. 32637, 2022, p. 1.

Burns, E., Svinkin, D., Fenimore, E., et al. 2023, *ApJ*, 946, L31. doi:10.3847/2041-8213/acc39c

Dichiara, S., et al. "Swift J1913.1+1946: a new bright hard X-ray and optical transient." GRB Coordinates Network, no. 32632, 2022, p. 1.

Edvige Ravasio, M., Sharan Salafia, O., Oganesyan, G., et al. 2023, arXiv:2303.16223. doi:10.48550/arXiv.2303.16223

Frederiks, D., et al. "Konus-Wind detection of GRB 221009A." GRB Coordinates Network, no. 32668, 2022, p. 1.

Gotz, D., et al. "GRB221009A/Swift J1913.1+1946: INTEGRAL SPI/ACS observations." GRB Coordinates Network, no. 32660, 2022, p. 1.

Huang, Y., et al. "LHAASO observed GRB 221009A with more than 5000 VHE photons up to around 18 TeV." GRB Coordinates Network, no. 32677, 2022, p. 1.

Kann, D. A., Agayeva, S., Aivazyan, V., et al. 2023, *ApJ*, 948, L12. doi:10.3847/2041-8213/acc8d0

Kumar, P. & Panaiteescu, A. 2000, *ApJ*, 541, L51. doi:10.1086/312905

Landau, L. D., Lifshitz, E. M. 2002, *The Classical Theory of Fields*, Vol. 2 (4th ed.; Oxford: Butterworth-Heinemann)

LHAASO Collaboration, Cao, Z., Aharonian, F., et al. 2023, *Science*, 380, 1390. doi:10.1126/science.adg9328

Lesage, S., et al. "GRB 221009A: Fermi GBM observation." GRB Coordinates Network, no. 32642, 2022, p. 1.

Malesani, D. B., Levan, A. J., Izzo, L., et al. 2023, arXiv:2302.07891. doi:10.48550/arXiv.2302.07891

Pe'er, A. & Zhang, B. 2024, arXiv:2407.16241. doi:10.48550/arXiv.2407.16241

Luigi Piro, Markus Ahlers, Alexis Coleiro, et al. 2022, *Experimental Astronomy*, 54, 23-117

Ruffini, R., Salmonson, J. D., Wilson, J. R., & Xue, S.-S. 1999, *Astron. Astrophys.*, 350, 334.

Ruffini, R., Salmonson, J. D., Wilson, J. R., & Xue, S.-S. 2000, *Astron. Astrophys.*, 359, 855.

Salafia, O. S., Ghisellini, G., Pescalli, A., et al. 2015, *MNRAS*, 450, 3549. doi:10.1093/mnras/stv766

Tan, W. J., et al. "Insight-HXMT observation of GRB221009A/Swift J1913.1+1946." *The Astronomer's Telegram*, no. 15660, 2022, p. 1.

Uhm, Z. L., & Zhang, B. 2014, *Nature Phys.*, 10, 351

Ursi, A., et al. "GRB 221009A (Swift J1913.1+1946): AGILE/MCAL detection." GRB Coordinates Network, no. 32650, 2022, p. 1.

Veres, P., et al. "GRB 221009A: Fermi GBM detection of an extraordinarily bright GRB." GRB Coordinates Network, no. 32636, 2022, p. 1.

Wei, Y.-J., Ren, J., He, H.-N., et al. 2024, *ApJ*, 968, L5. doi:10.3847/2041-8213/ad4ce1

Yuan, W., Zhang, C., Chen, Y., et al. 2022, *Handbook of X-ray and Gamma-ray Astrophysics*, 86. doi:10.1007/978-981-16-4544-0_151-1

Zhang, Y.-Q., Xiong, S.-L., Mao, J.-R., et al. 2024, *Science China Physics, Mechanics, and Astronomy*, 67, 289511. doi:10.1007/s11433-023-2381-0

Zhang, Z., Lin, H., Li, Z., et al. 2024, arXiv:2405.12977. doi:10.48550/arXiv.2405.12977

Zhang, B. 2019, *The Physics of Gamma-Ray Bursts* (New York, NY: Cambridge University Press), 217–220

Zheng, C., Zhang, Y.-Q., Xiong, S.-L., et al. 2024, *ApJ*, 962, L2. doi:10.3847/2041-8213/ad2073

Table B2. GRB candidates which could have e^-/e^+ production in their prompt emission stages, according to criterion equation (24), assuming $R_{\text{prod},16} = 0.3$

GRB	z	T_{90} (s)	$E_{p,i}$ (keV)	E_{iso} (10^{52} erg)	Detector
970828	0.96	146.59	586.0	30.38	GRO
971214	3.42	6.00	685.0	22.06	SAX
990123	1.60	61.00	1724.0	242.38	SAX/GRO/KW
990506	1.30	129.00	677.0	98.13	SAX/GRO/KW
990510	1.62	57.00	423.0	17.99	SAX
990705	0.84	32.00	459.0	18.70	SAX/KW
991208	0.71	63.10	313.0	22.97	KW
991216	1.02	45.00	648.0	69.79	SAX/GRO/KW
000131	4.50	96.30	987.0	181.48	GRO
000418	1.12	2.00	284.0	9.51	GRO
000911	1.06	23.30	1856.0	69.86	GRO
000926	2.04	54.70	310.0	27.98	GRO
010222	1.48	74.00	766.0	85.57	GRO
011211	2.14	51.00	186.0	5.71	GRO
020124	3.19	51.17	448.0	27.02	GRO
020405	0.69	40.00	354.0	10.64	GRO
020813	1.26	87.34	590.0	68.35	GRO
030226	1.99	76.23	289.0	12.94	GRO
030328	1.52	138.27	328.0	39.42	GRO
030528	0.78	62.80	57.0	2.22	GRO
040912	1.56	9.21	44.0	1.36	GRO
041006	0.72	22.08	98.0	3.11	GRO
050401	2.89	33.30	467.0	36.39	GRO
050603	2.82	11.08	1333.0	64.03	GRO
050814	5.30	144.00	339.0	11.20	GRO
050820	2.61	26.00	1325.0	102.89	GRO
050904	6.29	181.70	3178.0	127.35	GRO
051008	2.77	64.00	2074.0	83.40	GRO
051022	0.81	178.00	754.0	56.04	GRO
060124	2.29	658.20	784.0	43.85	GRO
060210	3.91	242.18	575.0	41.53	GRO
060510B	4.90	262.95	575.0	36.70	SWI
060714	2.71	116.04	234.0	13.40	SWI
060814	1.92	144.95	751.0	56.71	SWI
060906	3.69	44.58	209.0	14.90	SWI
060927	5.46	22.42	475.0	14.49	SWI
061007	1.26	75.74	890.0	89.96	SWI
061222A	2.09	96.00	874.0	30.04	SWI
061222B	3.36	37.25	200.0	10.30	SWI
070125	1.55	70.00	934.0	84.62	KW
070328	2.06	72.12	1182.0	77.70	KW
080319B	0.94	124.86	1261.0	117.87	SWI/KW